Supporting Information: Fine Structure of Excitons in Vacancy Ordered Halide Double Perovskites

Bruno Cucco,[†] Claudine Katan,[†] Jacky Even,[‡] Mikaël Kepenekian,[*,†] and George Volonakis[*,†]

[†]*Univ Rennes, ENSCR, INSA Rennes, CNRS, ISCR (Institut des Sciences Chimiques de Rennes), UMR 6226, France*

[‡]*Univ Rennes, INSA Rennes, CNRS, Institut FOTON - UMR 6082, Rennes, France*

E-mail: mikael.kepenekian@univ-rennes1.fr; yorgos.volonakis@univ-rennes1.fr

Computational Methods

All the calculations within the DFT framework are performed using the Quantum ESPRESSO Suite.[1,2] Structures are optimized with a 90 Ry cutoff for the plane-wave kinetic energy with a $8 \times 8 \times 8$ Brillouin zone sampling. The threshold on forces and total energy during ionic minimization were converged to 10^{-6} and 10^{-11}, respectively. During the optimization a 0.1 Kbar threshold is employed for the pressure on the variable cell. A threshold of 10^{-11} is employed for the SCF steps. All the calculations are performed using fully-relativistic norm-conserving PBE pseudopotential[3] taken from the pseudo-dojo database (http://www.pseudo-dojo.org). The phonon calculations are performed within the DFPT framework as also implemented in Quantum ESPRESSO. A $4 \times 4 \times 4$ k-grid is employed for the SCF, while the phonons are solved in a $2 \times 2 \times 2$ q-grid. A 10^{-16} threshold for phonon self-consistency is employed. For the electronic band structure symmetry analysis, we assume a cubic structure for Cs_2SnI_6 due to the structural and energetic similarities between the perfectly cubic crystalline structure and the distorted/rotated one. The total energy difference between the perfectly cubic and slightly tilted Cs_2SnI_6 is smaller than 1 meV/atom. The G_0W_0 calculations are performed on a $6 \times 6 \times 6$ k-grid sampling using the Rojas-Godby-Needs plasmon pole model to treat the frequency-dependent dielectric function.[4] Spin-orbit coupling is accounted non-perturbatively. We employ the equivalent of 15 Ry cutoff to set number of G vectors to be summed in the expression of the exchange self-energy, alongside a 8 Ry cutoff for the dielectric function calculation. We also include 400 bands for the sum over state summation in the GW correlation self-energy term. We included 600 polarization function bands for the calculation of the static dielectric screening. Optical absorption calculations are performed using the YAMBO[5] code. Calculation are performed within the Bethe-Salpeter formalism for e-h coupling and also IP approach. The BSE is solved within the Tamm-Dancoff approximation[6] on top of the G_0W_0 calculations by direct diagonalization on a uniform $6 \times 6 \times 6$ k-grid with 26 included bands around the band edges. We employ a cutoff of 10 Ry and 2 Ry for the summations on the reciprocal lattice vectors which appear in the exchange and attraction terms of the kernel, respectively. The calculations are performed using the same static dielectric screening from GW.

For the exciton spacial distribution, the hole position r_h is fixed close to the halogen atoms. This assumption comes from the fact that the VBM of these compounds is mainly composed by halogen-p orbitals. The G_0W_0 band structures were interpolated with Wannier90[7] on a dense $50 \times 50 \times 50$ k-grid to evaluate accurate effective masses. The orbitals composing the VBM and CBM of each material were used as basis to construct the Wannier functions. The effective masses were obtained by applying finite differences method to the Wannier interpolated band structures, as implemented on the WannierTools[8] software package.

Bethe-Salpeter Equation

The electron-hole interactions are included via the BSE equation which can be written in the space of transitions between valence and conduction states as a pseudo-eigenvalue problem for a two-particle Hamiltonian as follows

$$H^{vck}_{v'c'k'} = (\varepsilon_{ck} - \varepsilon_{vk})\delta_{vv'}\delta_{cc'}\delta_{kk'} + (f_{ck} - f_{vk})[2\bar{V}^{vck}_{v'c'k'} - W^{vck}_{v'c'k'}] \tag{1}$$

where v, c and k are indicating valence, conduction and momentum indexes, f_{ck} and f_{vk} are Fermi distribution functions, and $\bar{V}^{vck}_{v'c'k'}$ and $W^{vck}_{v'c'k'}$ are the electron-hole exchange and attraction part of the BSE kernel. To best describe the quasiparticle energies entering in the BSE kernel we perform the solution based on our previously discussed G_0W_0 calculations, allowing us to take into account the band-gap renormalization and dispersion corrections due to the formation of GW quasi-particles. For the calculations without e-h exchange interactions the $\bar{V}^{vck}_{v'c'k'}$ term is neglected.

Wannier-Mott Model

The Wannier-Mott (WM) exciton is usually found in semiconductors with small band-gaps and high dielectric constants. As a result, the Coulomb interactions between electrons and holes are strongly screened leading to small binding energies and a delocalization of the exciton wavefunction. Within the WM model, the binding energies and exciton bohr radius are obtained via the following equations

$$E^b_{WM} = -\frac{\mu Ry}{m_0 \varepsilon^2_\infty} \tag{2}$$

$$r_{WM} = \varepsilon_\infty \frac{m_0}{\mu} a_b \tag{3}$$

where μ represents the reduced effective mass, ε is the dielectric constant, R_y is the Rydberg constant and a_b is the Bohr radius.

Tables

Table S1: Structural parameters optimized within DFT-PBE. Here, a and a_{exp} are the theoretical and experimental lattice parameters, respectively, d_{M-X} is the bond-length between the metal site and halide, and V_{vac} is the volume of the vacancy-site, which is defined as the volume of the ΔX_6 octahedron. (M is the metal-site, Δ the vacancy-site and X the halogens).

M-site valency	s^0		p^0		d^0	
Compounds	Cs_2SnBr_6	Cs_2SnI_6	Cs_2TeBr_6	Cs_2TeI_6	Cs_2ZrBr_6	Cs_2ZrI_6
a (Å)	11.14	12.02	11.32	12.08	11.24	12.00
a_{exp} (Å)	10.86[9]	11.62[10]	10.91[11]	11.70[12]	11.16[13]	11.66[14]
d_{M-X} (Å)	2.65	2.91	2.74	2.98	2.65	2.88
V_{vac} (Å^3)	33.2	38.3	34.9	40.4	33.1	40.2

Table S2: Summary of the predicted electronic band-gaps within DFT and G_0W_0.

Compound	Cs_2SnBr_6	Cs_2SnI_6	Cs_2TeBr_6	Cs_2TeI_6	Cs_2ZrBr_6	Cs_2ZrI_6
DFT (eV)	1.30	0.17	2.04	1.16	2.73	1.65
G_0W_0 (eV)	3.65	1.51	3.66	2.63	5.02	3.32

Table S3: Charge carrier effective masses at the band edges within DFT and G_0W_0. Here we adopt the standard definitions of light and heavy effective masses for double degenerate bands, and fast and slow transport directions. Numbers inside parenthesis represents the heavy bands, while numbers inside square brackets represents the slow direction.

Effective masses(me)	Cs_2SnBr_6	Cs_2SnI_6	Cs_2TeBr_6	Cs_2TeI_6	Cs_2ZrBr_6	Cs_2ZrI_6
me^*_{GW}	0.24	0.29	0.29 [0.50]	0.33 [0.67]	1.27 [11.29]	0.86 [11.55]
mh^*_{GW}	0.55 (1.22)	0.58 (1.08)	0.31 [12.0]	0.20 [9.29]	1.12 (2.82)	0.60 (1.45)
me^*_{DFT}	0.26	0.30	0.25 [0.46]	0.15 [1.27]	0.95 [3.71]	0.66 [3.25]
mh^*_{DFT}	0.66 (1.60)	0.70 (1.38)	0.81 [11.2]	0.43 [0.65]	1.26 (3.25)	0.74 (1.90)

Table S4: Exciton binding energies E^b_{BSE} and dark-bright splitting (Δ_{db}) obtained from BSE@G_0W_0. The exciton binding energy is defined as the energy difference between the first direct dipole-allowed electronic transition and the first bright excitonic peak. The parameters employed for the Wannier-Mott model are also shown. Number between parenthesis represents the calculation with heavy effective masses.

Compound	Cs_2SnBr_6	Cs_2SnI_6	Cs_2TeBr_6	Cs_2TeI_6	Cs_2ZrBr_6	Cs_2ZrI_6
E^b_{BSE} (eV)	0.510	0.190	1.240	0.530	0.780	0.540
Δ_{db} (meV)	6	4	155	71	34	24
ε_∞	3.30	4.84	3.62	4.81	3.20	4.02
me^*_{GW}	0.24	0.29	0.29 [0.50]	0.33 [0.67]	1.23 (4.17)	0.85 (3.20)
mh^*_{GW}	0.37 (0.77)	0.54 (0.65)	0.22 [1.80]	0.21 [2.30]	0.61 (1.10)	0.33 (0.48)
μ	0.182	0.200	0.161	0.185	0.870	0.417
E^b_{WM} (eV)	0.228	0.116	0.167	0.109	1.156	0.351
r_{WM} (Å)	9.54	12.76	11.83	13.69	1.94	5.04

Figures

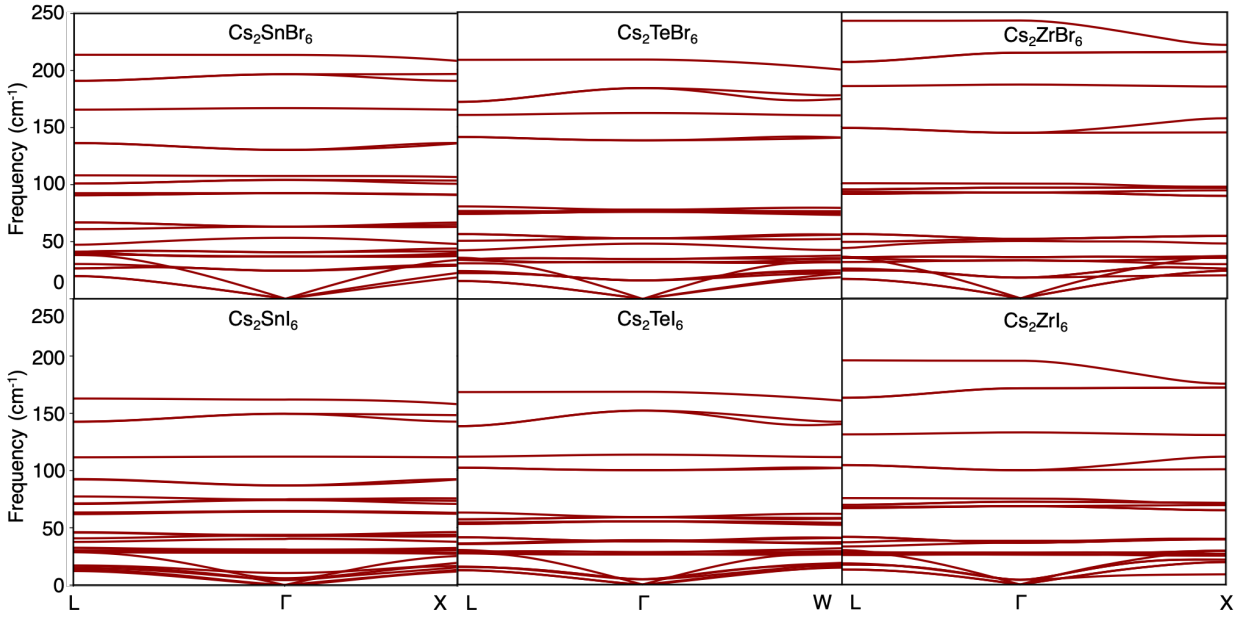

Figure S1: Phonon dispersion of optimized structures. The absence of imaginary (or soft) modes indicate mechanical stability.

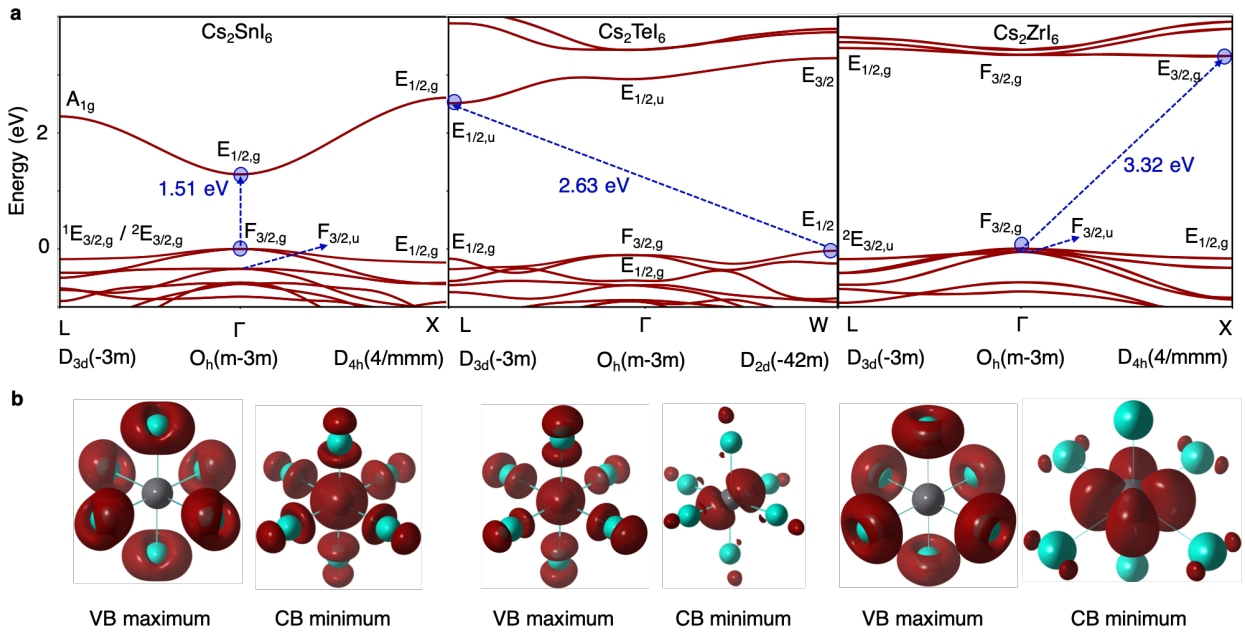

Figure S2: (a) G_0W_0 electronic band structures and charge densities. The irreducible representations and point group symmetries are shown and the valence band maximum (VBM) and conduction band minimum (CBM) are marked with blue circles. (b) Charge densities calculated at the VBM and CBM for the iodides.

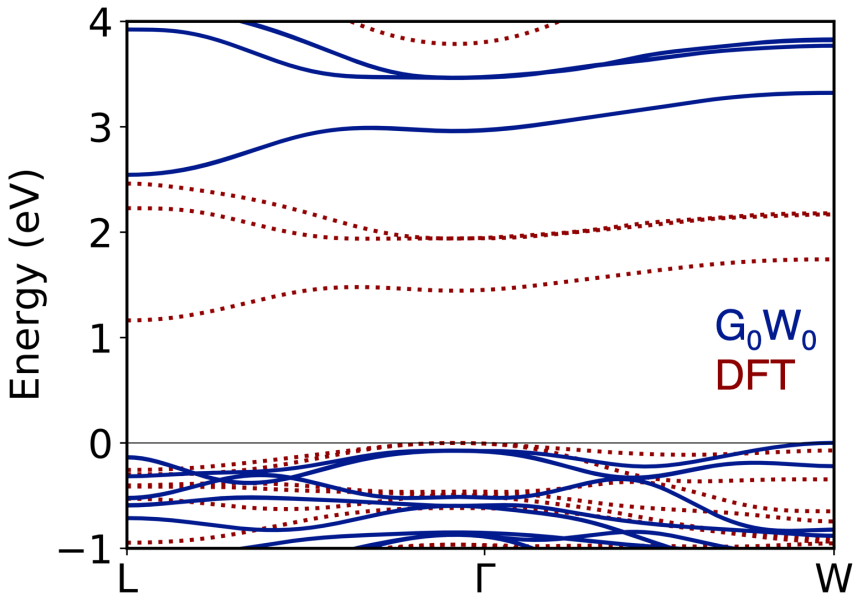

Figure S3: Calculated band structure of Cs_2TeI_6. The G_0W_0 bands are show in blue solid lines, while the DFT is show in red dotted lines. The black line at zero points the Fermi level.

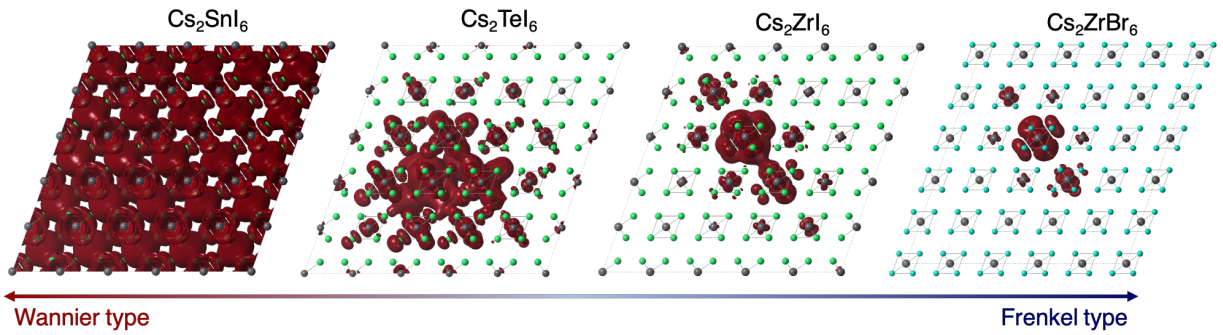

Figure S4: Exciton spatial distribution $|\Psi(r_h, r_e)|^2$ for the bright exciton of Cs_2SnI_6, Cs_2TeI_6, Cs_2ZrI_6 and Cs_2ZrBr_6. The hole position r_h is fixed in the vicinity of the halogen atoms. The wavefunctions are plotted using 85% of the maximum isovalue.

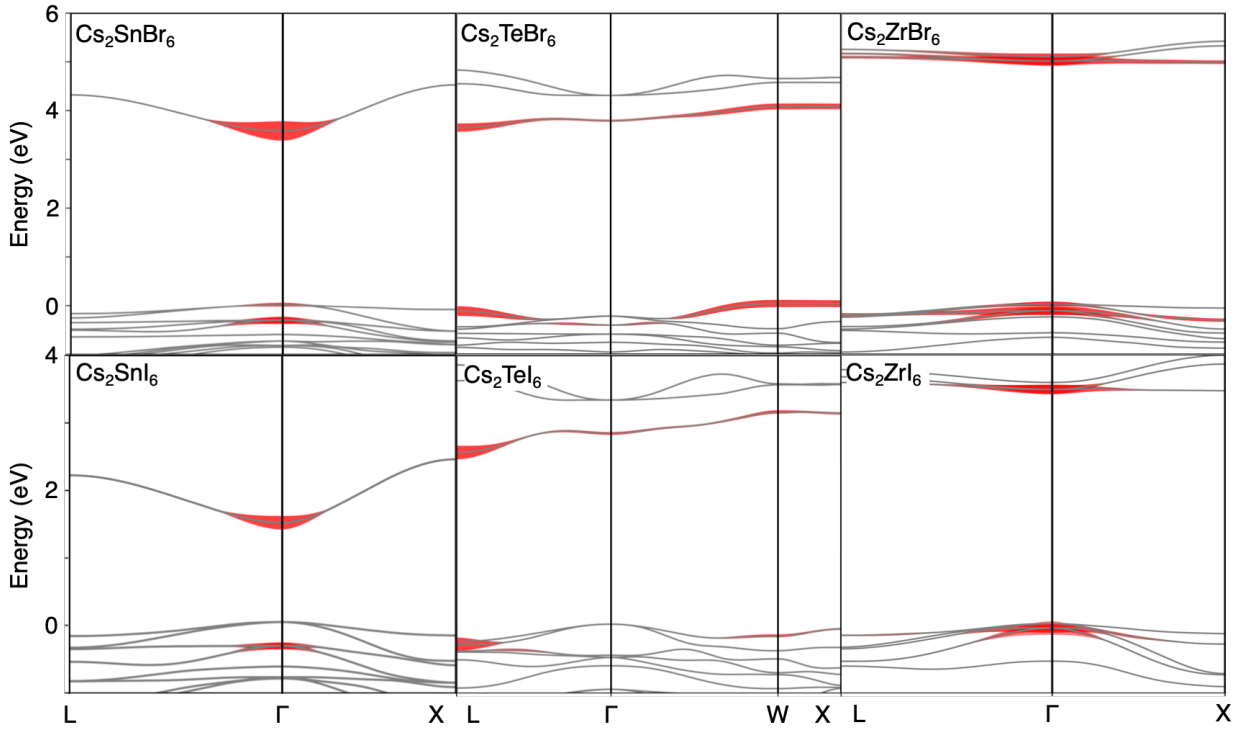

Figure S5: Projection of the weights $|A^{\lambda}_{eh}|$ over the DFT-PBE band structure. The band-gaps are rigidly shifted to match the G_0W_0 calculation. Here $|A^{\lambda}_{eh}|$ represents the expansion coefficient of the first bright exciton eigenvectors in terms of the electron-hole pairs $|eh\rangle$, i.e. $|\lambda\rangle = \sum_{eh} A^{\lambda}_{eh} |eh\rangle$.

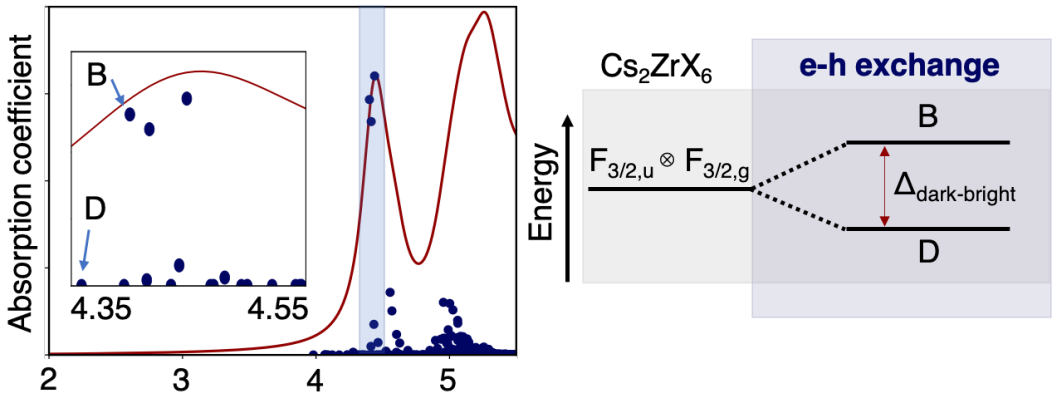

Figure S6: Cs_2ZrBr_6 calculated exciton oscillator strength with fine structure shown as inset plot. On the right, an illustration of the dark-bright splitting

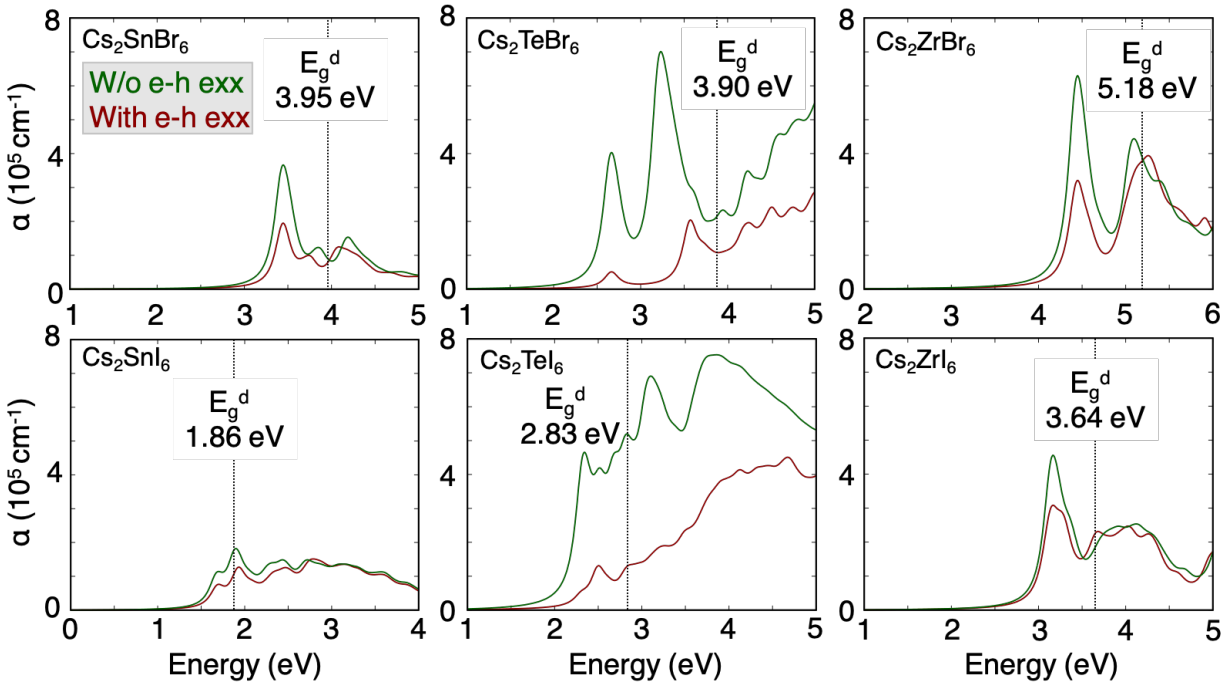

Figure S7: Comparison between the absorption coefficient obtained from solving the BSE with and without the inclusion of the e-h exchange interaction term $\bar{V}^{vck}_{v'c'k'}$ show in Equation S1. The black dotted lines show the position of the first direct dipole-allowed transition E_g^d at G_0W_0 level.

References

(1) Giannozzi, P.; Andreussi, O.; Brumme, T.; Bunau, O.; Nardelli, M. B.; Calandra, M.; Car, R.; Cavazzoni, C.; Ceresoli, D.; Cococcioni, M. et al. Advanced Capabilities for Materials Modelling with Quantum ESPRESSO. *J. Phys. Condens. Matter* **2017**, *29*, 465901.

(2) Giannozzi, P.; Baroni, S.; Bonini, N.; Calandra, M.; Car, R.; Cavazzoni, C.; Ceresoli, D.; Chiarotti, G. L.; Cococcioni, M.; Dabo, I. et al. QUANTUM ESPRESSO: A Modular and Open-Source Software Project for Quantum Simulations of Materials. *J. Phys. Condens. Matter.* **2009**, *21*, 395502.

(3) van Setten, M.; Giantomassi, M.; Bousquet, E.; Verstraete, M.; Hamann, D.; Gonze, X.; Rignanese, G.-M. The PseudoDojo: Training and Grading a 85 Element Optimized Norm-conserving Pseudopotential Table. *Comput. Phys. Commun.* **2018**, *226*, 39–54.

(4) Rojas, H. N.; Godby, R. W.; Needs, R. J. Space-Time Method for Ab Initio Calculations of Self-Energies and Dielectric Response Functions of Solids. *Phys. Rev. Lett.* **1995**, *74*, 1827–1830.

(5) Sangalli, D.; Ferretti, A.; Miranda, H.; Attaccalite, C.; Marri, I.; Cannuccia, E.; Melo, P.; Marsili, M.; Paleari, F.; Marrazzo, A. et al. Many-body Perturbation Theory Calculations Using the Yambo Code. *J. Phys. Condens. Matter* **2019**, *31*, 325902.

(6) Kronik, L.; Neaton, J. B. Excited-State Properties of Molecular Solids from First Principles. *Annu. Rev. Phys. Chem.* **2016**, *67*, 587–616.

(7) Mostofi, A. A.; Yates, J. R.; Pizzi, G.; Lee, Y.-S.; Souza, I.; Vanderbilt, D.; Marzari, N. An Updated Version of Wannier90: A tool for Obtaining Maximally-Localised Wannier Functions. *Comput. Phys. Commun.* **2014**, *185*, 2309–2310.

(8) Wu, Q.; Zhang, S.; Song, H.-F.; Troyer, M.; Soluyanov, A. A. WannierTools : An Open-

Source Software Package for Novel Topological Materials. *Comput. Phys. Commun.* **2018**, *224*, 405 – 416.

(9) Kaltzoglou, A.; Antoniadou, M.; Kontos, A. G.; Stoumpos, C. C.; Perganti, D.; Siranidi, E.; Raptis, V.; Trohidou, K.; Psycharis, V.; Kanatzidis, M. G. et al. Optical-Vibrational Properties of the Cs_2SnX_6 (X = Cl, Br, I) Defect Perovskites and Hole-Transport Efficiency in Dye-Sensitized Solar Cells. *J. Phys. Chem. C* **2016**, *120*, 11777–11785.

(10) Lee, B.; Stoumpos, C. C.; Zhou, N.; Hao, F.; Malliakas, C.; Yeh, C.-Y.; Marks, T. J.; Kanatzidis, M. G.; Chang, R. P. H. Air-Stable Molecular Semiconducting Iodosalts for Solar Cell Applications: Cs_2SnI_6 as a Hole Conductor. *J. Am. Chem. Soc.* **2014**, *136*, 15379–15385.

(11) Folgueras, M. C.; Jin, J.; Gao, M.; Quan, L. N.; Steele, J. A.; Srivastava, S.; Ross, M. B.; Zhang, R.; Seeler, F.; Schierle-Arndt, K. et al. Lattice Dynamics and Optoelectronic Properties of Vacancy-Ordered Double Perovskite Cs_2TeX_6 (X = Cl–, Br–, I–) Single Crystals. *J. Phys. Chem. C* **2021**, *125*, 25126–25139.

(12) Maughan, A. E.; Ganose, A. M.; Bordelon, M. M.; Miller, E. M.; Scanlon, D. O.; Neilson, J. R. Defect Tolerance to Intolerance in the Vacancy-Ordered Double Perovskite Semiconductors Cs_2SnI_6 and Cs_2TeI_6. *J. Am. Chem. Soc.* **2016**, *138*, 8453–8464.

(13) Abfalterer, A.; Shamsi, J.; Kubicki, D. J.; Savory, C. N.; Xiao, J.; Divitini, G.; Li, W.; Macpherson, S.; Gałkowski, K.; MacManus-Driscoll, J. L. et al. Colloidal Synthesis and Optical Properties of Perovskite-Inspired Cesium Zirconium Halide Nanocrystals. *ACS Mater. Lett.* **2020**, *2*, 1644–1652.

(14) Guthrie, D. H.; Corbett, J. D. Two Zirconium Iodide Clusters. Hexazirconium Dodecaiodide (Zr_6I_{12}) and Cesium Hexazirconium Tetradecaiodide ($CsZr_6I_{14}$). *Inorg. Chem.* **1982**, *21*, 3290–3295.